LETTER

doi:10.1038/nature13184

Ultralow thermal conductivity and high thermoelectric figure of merit in SnSe crystals

Li-Dong Zhao[1], Shih-Han Lo[2], Yongsheng Zhang[2], Hui Sun[3], Gangjian Tan[1], Ctirad Uher[3], C. Wolverton[2], Vinayak P. Dravid[2] & Mercouri G. Kanatzidis[1]

The thermoelectric effect enables direct and reversible conversion between thermal and electrical energy, and provides a viable route for power generation from waste heat. The efficiency of thermoelectric materials is dictated by the dimensionless figure of merit, *ZT* (where *Z* is the figure of merit and *T* is absolute temperature), which governs the Carnot efficiency for heat conversion. Enhancements above the generally high threshold value of 2.5 have important implications for commercial deployment[1,2], especially for compounds free of Pb and Te. Here we report an unprecedented *ZT* of 2.6 ± 0.3 at 923 K, realized in SnSe single crystals measured along the *b* axis of the room-temperature orthorhombic unit cell. This material also shows a high *ZT* of 2.3 ± 0.3 along the *c* axis but a significantly reduced *ZT* of 0.8 ± 0.2 along the *a* axis. We attribute the remarkably high *ZT* along the *b* axis to the intrinsically ultralow lattice thermal conductivity in SnSe. The layered structure of SnSe derives from a distorted rock-salt structure, and features anomalously high Grüneisen parameters, which reflect the anharmonic and anisotropic bonding. We attribute the exceptionally low lattice thermal conductivity (0.23 ± 0.03 W m^{-1} K^{-1} at 973 K) in SnSe to the anharmonicity. These findings highlight alternative strategies to nanostructuring for achieving high thermoelectric performance.

The efficiency of thermoelectric materials and devices is determined by the dimensionless figure of merit (*ZT*), defined as $ZT = (S^2\sigma/\kappa)T$, where S, σ and κ are the Seebeck coefficient, the electrical conductivity and the thermal conductivity, respectively[1,2]. The well-known interdependence of S, σ and κ complicates efforts to develop strategies for improving a material's average *ZT* well above 2.5, especially using less expensive, more Earth-abundant materials[2–4], a feat that could revolutionize the field of thermal energy conversion. Several approaches to enhance *ZT* have emerged in the past decade, including enhancement of Seebeck coefficients (by modifying the band structure[5], heavy valence (conduction) band convergence[6,7], quantum confinement effects[8] and electron energy barrier filtering[9]), and reducing lattice thermal conductivity (by nanostructuring[10] and all-scale hierarchical architecturing[11]) while maintaining hole mobility (band energy alignment between nano-precipitate and matrix[12–14]). Most of these approaches aim to maintain a high power factor (electrical transport properties) and/or reduce the lattice thermal conductivity. Alternatively, high performance could be sought in pristine thermoelectric compounds with intrinsically low thermal conductivity, which may arise from properties such as a large molecular weight[15], a complex crystal structure[16] or charge density wave distortions[17].

We find that SnSe, which is a very stable and simple compound consisting of Earth-abundant elements, exhibits an intrinsically ultralow thermal conductivity. Historically, SnSe was ignored by the thermoelectric community[18,19]; however, its layered and anisotropic crystal structure motivated us to explore its electrical transport properties along all axial directions (unless otherwise noted, all crystallographic directions and planes mentioned in this Letter are defined with respect to its room-temperature form, with *Pnma* space group, #62). Surprisingly, we find that the electrical resistivity is low enough to result in a moderate power factor (along the *b* axis), but, even more surprisingly, we observe that the thermal conductivity of SnSe is intrinsically ultralow (<0.25 W m^{-1} K^{-1} at >800 K), resulting in $ZT = 2.62$ at 923 K along the *b* axis and 2.3 along the *c* axis; these represent the highest *ZT* values reported so far for any thermoelectric system. Along the *a* direction, however, *ZT* is significantly lower, ~0.8. Here, it should be noted that SnSe along the *b* axis shows a room-temperature $ZT = 0.12$, which is comparable to the room-temperature value of 0.15 reported earlier[19]. SnSe, however, reveals high *ZT* values near and above the transition temperature of 750 K at which the structure converts from *Pnma* to *Cmcm*[20–22]. Such ultrahigh *ZT* along two principal directions and the observed crystallographic and *ZT* anisotropy prompted us to investigate the scientific underpinning of these intriguing results.

SnSe adopts a layered orthorhombic crystal structure at room temperature, which can be derived from a three-dimensional distortion of the NaCl structure. The perspective views of the room-temperature SnSe crystal structure along the *a*, *b* and *c* axial directions are shown in Fig. 1a–d. There are two-atom-thick SnSe slabs (along the *b*–*c* plane) with strong Sn–Se bonding within the plane of the slabs, which are then linked with weaker Sn–Se bonding along the *a* direction[20]. The structure contains highly distorted $SnSe_7$ coordination polyhedra, which have three short and four very long Sn–Se bonds, and a lone pair of the Sn^{2+} sterically accommodated between the four long Sn–Se bonds (Fig. 1b). The two-atom-thick SnSe slabs are corrugated, creating a zig-zag accordion-like projection along the *b* axis. The easy cleavage in this system is along the (l00) planes. While cooling from its high-temperature, higher symmetry phase (space group *Cmcm*, #63), SnSe undergoes a displacive (shear) phase transition at ~750–800 K, resulting in a lower symmetry *Pnma* (#62) space group and concomitant matrix transformation of its axes[21,22].

The *ZT* values along the three different crystallographic axes are shown in Fig. 1e. The inset of Fig. 1e shows the SnSe crystals and the cutting directions for typical samples in this study. It should be noted that the *a*, *b* and *c* axial directions were determined through X-ray diffraction (XRD; Extended Data Fig. 1) as well as electron backscatter diffraction (EBSD) analysis (Extended Data Fig. 2).

The electrical conductivities for SnSe crystals along different crystallographic directions show the same temperature-dependent trend (Fig. 2a). We observe three regions: first, metallic transport behaviour from 300 to 525 K; then a change to thermally activated semiconducting behaviour up to ~800 K; and above that, a nearly temperature-independent trend up to 973 K. The first upturn above 525 K is attributed to the thermal excitation of carriers, while the second is related to the phase transition from *Pnma* ($a = 11.49$ Å, $b = 4.44$ Å, $c = 4.135$ Å) to the *Cmcm* ($a = 4.31$ Å, $b = 11.70$ Å, $c = 4.31$ Å) space group[21,22]. It can be readily seen that the electrical conductivities along the *b* and *c* directions are similar, whereas it is lower along the *a* direction. This anisotropy is due to the higher ratio of Hall coefficient to resistivity, R_H/ρ (related to mobility), within the plane of the SnSe slabs than perpendicular to them (that is, along the *a* direction) (Extended Data Fig. 3). The Seebeck

[1]Department of Chemistry, Northwestern University, Evanston, Illinois 60208, USA. [2]Department of Materials Science and Engineering, Northwestern University, Evanston, Illinois 60208, USA. [3]Department of Physics, University of Michigan, Ann Arbor, Michigan 48109, USA.

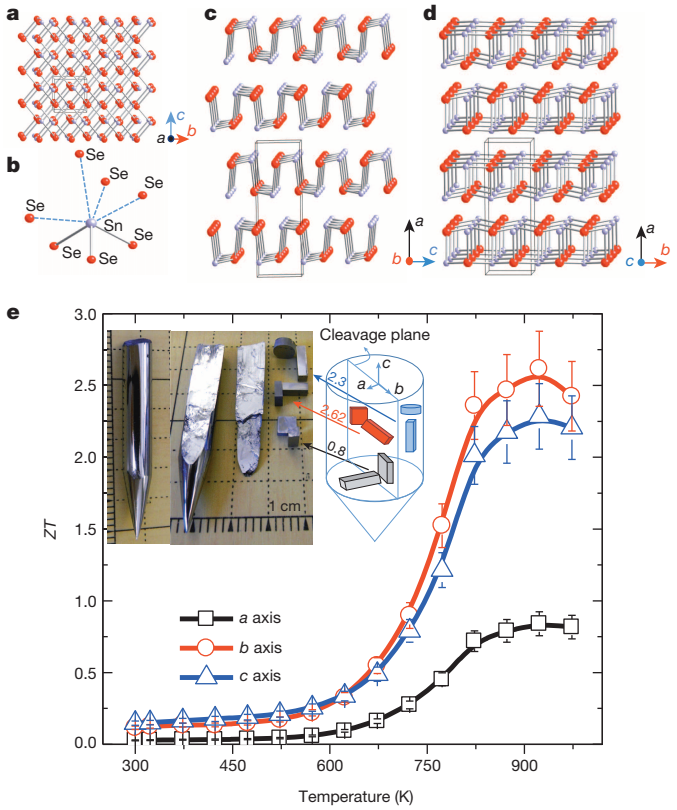

Figure 1 | SnSe crystal structure *Pnma* and *ZT* values. **a**, Crystal structure along the *a* axis: grey, Sn atoms; red, Se atoms. **b**, Highly distorted $SnSe_7$ coordination polyhedron with three short and four long Sn–Se bonds. **c**, Structure along the *b* axis. **d**, Structure along the *c* axis. **e**, Main panel, *ZT* values along different axial directions; the *ZT* measurement uncertainty is about 15% (error bars). Inset images: left, a typical crystal; right, a crystal cleaved along the (l00) plane, and specimens cut along the three axes and corresponding measurement directions. Inset diagram, how crystals were cut for directional measurements; *ZT* values are shown on the blue, red and grey arrows; colours represent specimens oriented in different directions.

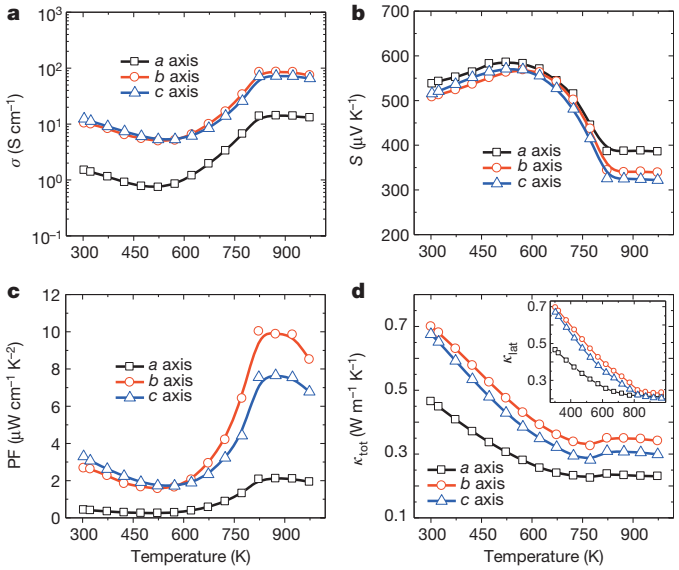

Figure 2 | Thermoelectric properties as a function of temperature for SnSe crystals. **a**, Electrical conductivity. **b**, Seebeck coefficient. **c**, Power factor, PF. **d**, Total thermal conductivity, κ_{tot}. Inset, lattice thermal conductivity, κ_{lat} (same units as κ_{tot}), versus temperature (same units as main panel).

coefficients show almost isotropic behaviour, and are independent of crystallographic directions (Fig. 2b). The gradual decrease of the Seebeck coefficients above 525 K is consistent with the increasing trend in the electrical conductivity, and suggests bipolar conduction and an increasing inverse Hall coefficient, $1/R_H$ (Extended Data Fig. 3a). This behaviour is consistent with our electronic band structure calculations (Extended Data Fig. 4), which show that the bandgap (E_g) decreases considerably from *Pnma* (0.61 eV) to *Cmcm* (0.39 eV), and thus a bipolar conduction process is expected with rising temperature.

The power factor along the *b* axis shows the highest value (10.1 μW $cm^{-1} K^{-2}$) compared to the other two axial directions around 850 K (Fig. 2c); the maximum power factors at 850 K along the *c* and *a* directions are 7.7 μW $cm^{-1} K^{-2}$ and 2.1 μW $cm^{-1} K^{-2}$, respectively. Compared to other state-of-the-art thermoelectrics[2–4], the power factors obtained in SnSe crystals are moderate, but are much higher than those found in other thermoelectrics with intrinsically low overall thermal conductivity (for example, $Yb_{14}MnSb_{11}$, Ag_9TlTe_5, $AgSbTe_2$)[15,16,23]. The highest power factor along *b* is in agreement with the highest R_H/ρ of 250 $cm^2 V^{-1} s^{-1}$ obtained along this axis, which is twofold higher than that along the *c* axis, and tenfold higher than that along the *a* axis (Extended Data Fig. 3b).

The temperature dependence of total thermal conductivity (κ_{tot}) is shown in Fig. 2d. At room temperature (~300 K), the values of κ_{tot} are (in W $m^{-1} K^{-1}$) ~0.46, 0.70 and 0.68 along the *a*, *b* and *c* axis directions, respectively. Compared to state-of-the-art thermoelectrics[2–4], these thermal conductivity values are exceedingly low. Surprisingly, these low values continue to decrease with rising temperature, and at 973 K all fall in the range 0.23–0.34 W $m^{-1} K^{-1}$. The ratio of lattice thermal conductivity (κ_{lat}) to κ_{tot} indicates that κ_{tot} is dominated by phonon transport (Extended Data Fig. 6d). The inset in Fig. 2d indicates that κ_{lat} falls as low as 0.20 W $m^{-1} K^{-1}$ at 973 K along the *a* direction. This is a remarkably low value, which is lower than those obtained even by nanostructuring and all-scale hierarchical architecturing of PbTe-based thermoelectric materials[11].

The dynamic structural behaviour of SnSe above 750 K, involving a reversible phase transition from low-temperature *Pnma* to a high-temperature *Cmcm* space group, helps to preserve the high power factor[22]. This is because the *Cmcm* phase, which is structurally closely related to the *Pnma* phase, exhibits a substantially reduced energy gap and enhanced carrier mobilities while maintaining the ultralow thermal conductivity. We have confirmed this transition using *in situ* sample heating in a transmission electron microscope (TEM). A defect-free lattice image of a SnSe specimen is shown in Fig. 3a, with the inset showing the corresponding selected area diffraction (SAD) pattern taken along the [011] zone axis. It should be noted that kinematically forbidden reflections for the *Pnma* space group, of the type {100}, occur owing to ubiquitous double diffraction in electron diffraction along these directions, and reflect the presence of translational symmetry elements (screw axes/glide planes) in the space group[24]. Other detailed crystal information, including high-resolution TEM images along multiple crystal orientations ([100], [201], [211], [021]) and SAD along [001] and [010], are shown in Extended Data Fig. 7, which confirms the single-crystal SnSe phase at room temperature.

We used the SAD mode (obtained after zone axis alignment with convergent beam electron diffraction) because it is sensitive and can detect subtle changes in crystal symmetry, especially angular rotations. The [211] zone axis at room temperature, which becomes the [121] zone after the transition at about 750–800 K, was chosen to resolve the evolution of the planes (1−1−1) and (0−11). As illustrated by the crystal models in Fig. 3b, viewing along [211] and [121] at room temperature and high temperature, respectively, the plane normal angle between (1−1−1) and (0−11) (marked as blue lines) is expected to change from 86.18° to 89.89° on transition. Figure 3c shows this variation of the angle on the experimentally determined SADs, and we see a good match with the simulated SADs in Extended Data Fig. 8. The diffraction patterns in Fig. 3c were obtained from the same sample area. The sample temperature was

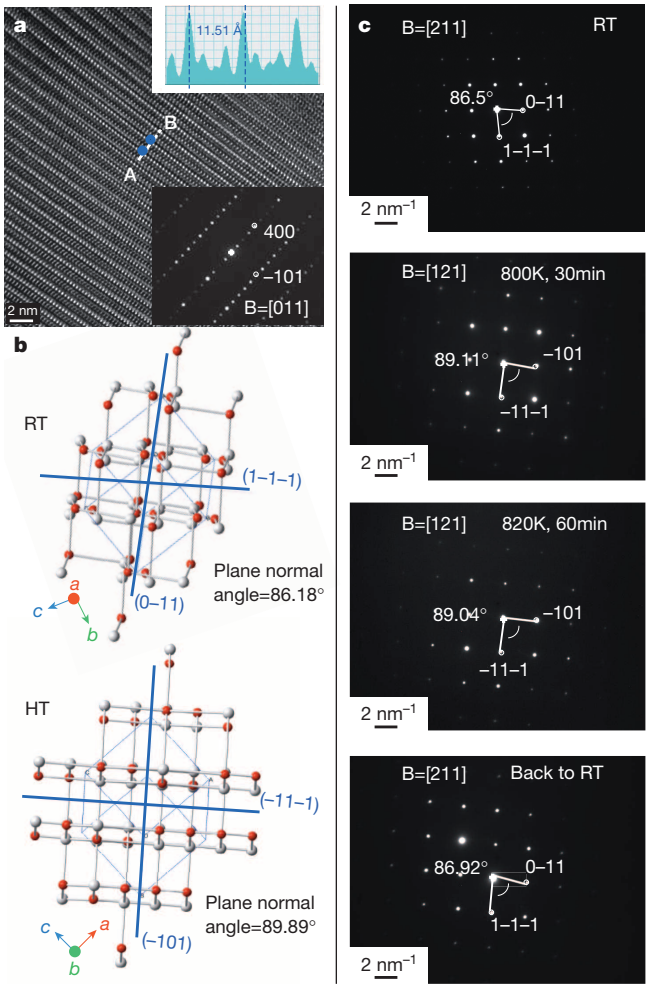

Figure 3 | High-temperature *in situ* TEM observations. **a**, Main panel, high-resolution TEM image of single-crystal SnSe (scale bar, 2 nm). Bottom inset, corresponding diffraction pattern along the [011] zone axis; top inset, the line profile (distance is plotted in Å, *y* axis) along the dotted line AB in the main panel showing the *d* spacing of (100). **b**, Simulated crystal structures of the phase at room temperature (RT; *Pnma*) and at high temperature (HT; *Cmcm*), viewing along the [211] and [121] directions; planes (1−1−1), (−101) and (0−11) are marked by blue lines. **c**, Diffraction patterns obtained at different temperatures. B, zone axis. There is a difference in measured angle between (1−1−1) and (0−11) of about 2.6° between room and elevated temperatures.

increased rapidly from room temperature to 800 K, and then held at this temperature for 30 min after which a diffraction pattern was obtained; the temperature was then increased to 820 K, and the diffraction pattern determined again after holding at this temperature for 60 min; the sample was then brought back to room temperature and the pattern obtained again. The angle between (1−1−1) and (0−11) increased by 2.6° when 800 K was reached. The high-temperature phase is stable up to 820 K for the extended duration used here. There was no noticeable change in terms of *d* spacing and angles between the two SADs at elevated temperatures. In addition, the phase transition was observed to be reversible by returning to room temperature and monitoring the SAD of the *Pnma* phase that reappears. These observations are consistent with a displacive reversible phase transition between *Pnma* and *Cmcm* space groups at about 800 K. Given the subtle angular changes in diffraction observations, it is likely that the phase transition may involve mere shuffling of the SnSe layers, as expected for a displacive second-order phase transition and consistent with the very close relationship of the two structures.

It is known that strong anharmonicity in bonding can give rise to low lattice thermal conductivity in ordered crystal structures[23,25,26]. The strength of the lattice anharmonicity can be estimated from the Grüneisen parameters, which characterize the relationship between phonon frequency and crystal volume change. Therefore, to clarify the origin of the intrinsically low thermal conductivity of SnSe, the phonon and Grüneisen dispersions were calculated using first-principles density functional theory (DFT) phonon calculations within the quasi-harmonic approximation. Figure 4a shows that the acoustic modes along the Γ–X Brillouin zone direction (*a* axis) are significantly softer (with lower Debye temperatures and smaller phonon velocities; see Extended Data Table 1) than those along both the Γ–Y (*b* axis) and the Γ–Z Brillouin zone direction (*c* axis). These soft modes along the *a* axis suggest weak interatomic bonding and possible strong anharmonicity. To quantitatively assess the anharmonicity along the three directions, we plot the dispersion of the Grüneisen parameters of SnSe (Fig. 4b), which shows that the Grüneisen parameters are all very large, with that along the *a* axis being

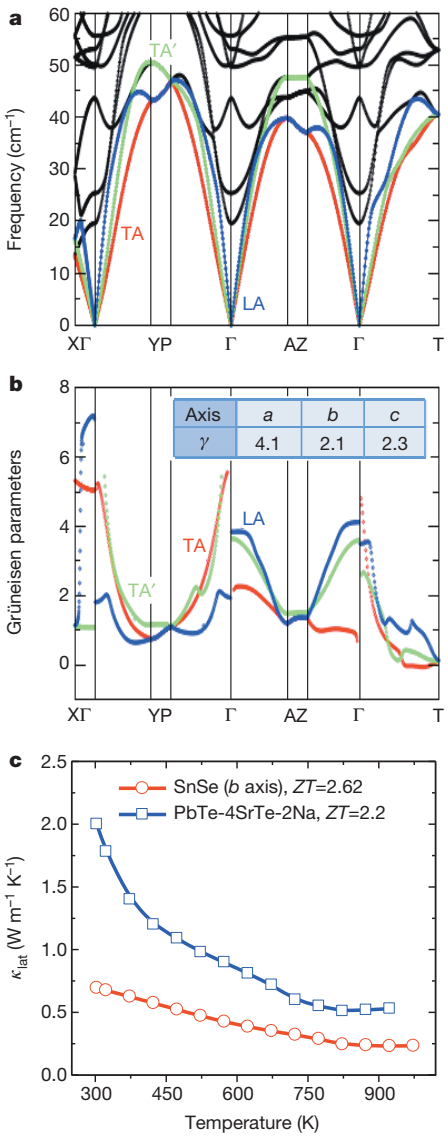

Figure 4 | Theoretically calculated phonon and Grüneisen dispersions, and measured lattice thermal conductivity. **a**, Phonon dispersion. TA, TA′, transverse acoustic phonon scattering branches; LA, longitudinal acoustic phonon scattering branch. **b**, Grüneisen dispersion; inset, the average Grüneisen parameters along *a*, *b* and *c* axes. TA, red colour; TA′, green colour; LA, blue colour. The high symmetry points in the first Brillouin zone can be found in Extended Data Fig. 4. **c**, The lattice thermal conductivity comparison of SnSe along the *b* axis (ZT_{max} = 2.62) and hierarchical architectured PbTe-4SrTe-2Na (ZT_{max} = 2.2)[11].

larger than those along both the *b* and *c* axes. The average Grüneisen parameters along the *a*, *b* and *c* axes are 4.1, 2.1 and 2.3, respectively, as shown in the inset of Fig. 4b. Along the *a* axis, the maximum longitudinal acoustic (LA) Grüneisen parameter around the Γ point is extraordinarily high, ~7.2. In contrast, the Grüneisen parameters are 2.05 for $AgSbTe_2$ (ref. 23), 3.5 for $AgSbSe_2$ (ref. 25) and 1.45 for PbTe (ref. 27), corresponding to measured lattice thermal conductivities at room temperature (in $W\,m^{-1}\,K^{-1}$) of 0.68, 0.48 and 2.4, respectively. The anomalously high Grüneisen parameter of SnSe is a reflection of its crystal structure, which contains very distorted $SnSe_7$ polyhedra (due to the lone pair of Sn^{2+}) and a zig-zag accordion-like geometry of slabs in the *b*–*c* plane. This implies a soft lattice—and if this lattice were mechanically stressed along the *b* and *c* directions, the Sn–Se bond length would not change directly, but instead the zig-zag geometry would be deformed like a retractable spring or an accordion. In addition, along the *a* direction, the weaker bonding between SnSe slabs provides a good stress buffer or 'cushion', thus dissipating phonon transport laterally[28]. The anomalously high Grüneisen parameter is therefore a consequence of the 'soft' bonding in SnSe, which leads to the very low lattice thermal conductivity.

Using our DFT-calculated quantities (Debye temperatures and phonon velocities; see Supplementary Table 1) in the amorphous limit equation[29], we can calculate the minimum lattice thermal conductivity of the three directions (*a*, *b* and *c* axis) at 770 K: $\kappa_{min}{}^{a} = 0.256\ W\,m^{-1}\,K^{-1}$, $\kappa_{min}{}^{b} = 0.360\ W\,m^{-1}\,K^{-1}$ and $\kappa_{min}{}^{c} = 0.326\ W\,m^{-1}\,K^{-1}$. The trend of the theoretically predicted minimum thermal conductivity κ_{min} is in good agreement with the experimental measurements ($\kappa_{lat}{}^{a} < \kappa_{lat}{}^{c} < \kappa_{lat}{}^{b}$). The theoretically calculated minimal thermal conductivities are slightly larger than those from experimental measurements, which could possibly result from (1) the value of the Lorenz number, $1.5 \times 10^{-8}\ V^2\,K^2$, which can vary in the range $(1–2.4) \times 10^{-8}\ V^2\,K^2$; (2) the values of thermal diffusivity, which depend on the details of a fit to time-dependent reflectivity curves (in which instrumental error is about 5%); (3) errors associated with the determined sample thickness, the homogeneity of that thickness, and the determined sample density; and (4) the difficulty of measuring precisely along one crystallographic axis. Indeed, the EBSD analysis shows an ~11° angular deviation of the crystallographic axes from the surface normal (Extended Data Fig. 2).

It is interesting to compare the lattice thermal conductivity of SnSe with that of state-of-the-art thermoelectric systems. The previously reported nanostructured all-scale hierarchical PbTe-4SrTe-2Na (with *ZT* of 2.2) exhibits a lattice thermal conductivity of $0.5\ W\,m^{-1}\,K^{-1}$ (see Fig. 4c)[11]. The unprecedented $ZT \approx 2.62$ of SnSe comes principally from an even lower lattice thermal conductivity of $0.23\ W\,m^{-1}\,K^{-1}$ despite the lack of nanostructuring. We find good experimental repeatability for this high *ZT*, as evidenced by measurements on seven separate crystals prepared independently (Extended Data Fig. 10).

The value of *ZT* (~2.62) at 923 K in SnSe crystals suggests that bulk materials with layered structures, anharmonic bonding and intrinsically ultralow thermal conductivity are promising candidates for providing high thermoelectric performance. It is remarkable that this ultralow thermal conductivity can be realized in a simple compound such as SnSe, as it does not have high molecular weight, a complex crystal structure or a large unit cell. These attributes are generally associated with low thermal conductivity. Compared to other high-performance thermoelectrics, our results for SnSe demonstrate that a high *ZT* also can be realized in simple layered, anisotropic and anharmonic systems, without nanostructuring.

METHODS SUMMARY

The SnSe samples were synthesized first in the form of ingots by heating to 1,223 K over 9.5 h, soaking at that temperature for 6 h, then furnace-cooling to room temperature, followed by vertical Bridgman crystal growth by heating to 1,223 K over 9.5 h, and then cooling from 1,223 K to room temperature with the sample moving at a rate of $2\ mm\,h^{-1}$. The electrical resistivity and Seebeck coefficient were measured simultaneously in a helium atmosphere at 300–973 K using a ULVAC-RIKO ZEM-3 instrument system. We determined carrier concentrations using a custom-made apparatus at 300–823 K. The thermal diffusivity, *D*, was directly measured at 300–973 K by using the laser flash diffusivity method in a commercial Netzsch LFA-457 instrument. The thermal diffusivity was measured along the same direction as the electrical transport. The heat capacity, C_p, was indirectly derived using a representative sample (Pyroceram 9606) in the range 300–973 K. The total thermal conductivity was calculated using the formula $\kappa = DC_p\rho$, where ρ is the sample density, which was determined using the dimensions and mass of the sample and then reconfirmed by measurements using a gas pycnometer (Micromeritics AccuPyc 1340). Transmission electron microscope (TEM) investigation was conducted with a JEOL 2100F at 200 kV. The phonon and Grüneisen dispersions were obtained by using first-principles DFT phonon calculations within the quasi-harmonic approximation.

Online Content Any additional Methods, Extended Data display items and Source Data are available in the online version of the paper; references unique to these sections appear only in the online paper.

Received 26 November 2013; accepted 24 February 2014.

1. Heremans, J. P., Dresselhaus, M. S., Bell, L. E. & Morelli, D. T. When thermoelectrics reached the nanoscale. *Nature Nanotechnol.* **8,** 471–473 (2013).
2. Zhao, L. D., Dravid, V. P. & Kanatzidis, M. G. The panoscopic approach to high performance thermoelectrics. *Energ. Environ. Sci.* **7,** 251–268 (2014).
3. Snyder, G. J. & Toberer, E. S. Complex thermoelectric materials. *Nature Mater.* **7,** 105–114 (2008).
4. Dresselhaus, M. S. *et al.* New directions for low-dimensional thermoelectric materials. *Adv. Mater.* **19,** 1043–1053 (2007).
5. Heremans, J. P. *et al.* Enhancement of thermoelectric efficiency in PbTe by distortion of the electronic density of states. *Science* **321,** 554–557 (2008).
6. Pei, Y. *et al.* Convergence of electronic bands for high performance bulk thermoelectrics. *Nature* **473,** 66–69 (2011).
7. Liu, W. *et al.* Convergence of conduction bands as a means of enhancing thermoelectric performance of *n*-type $Mg_2Si_{1-x}Sn_x$ solid solutions. *Phys. Rev. Lett.* **108,** 166601 (2012).
8. Hicks, L. D. & Dresselhaus, M. S. Effect of quantum-well structures on the thermoelectric figure of merit. *Phys. Rev. B* **47,** 12727–12731 (1993).
9. Heremans, J. P., Thrush, C. M. & Morelli, D. T. Thermopower enhancement in lead telluride nanostructures. *Phys. Rev. B* **70,** 115334 (2004).
10. Hsu, K. F. *et al.* Cubic $AgPb_mSbTe_{2+m}$: bulk thermoelectric materials with high figure of merit. *Science* **303,** 818–821 (2004).
11. Biswas, K. *et al.* High-performance bulk thermoelectrics with all-scale hierarchical architectures. *Nature* **489,** 414–418 (2012).
12. Biswas, K. *et al.* Strained endotaxial nanostructures with high thermoelectric figure of merit. *Nature Chem.* **3,** 160–166 (2011).
13. Zhao, L. D. *et al.* High thermoelectric performance *via* hierarchical compositionally alloyed nanostructures. *J. Am. Chem. Soc.* **135,** 7364–7370 (2013).
14. Zhao, L. D. *et al.* Raising the thermoelectric performance of *p*-type PbS with endotaxial nanostructuring and valence-band offset engineering using CdS and ZnS. *J. Am. Chem. Soc.* **134,** 16327–16336 (2012).
15. Brown, S. R., Kauzlarich, S. M., Gascoin, F. & Snyder, G. J. $Yb_{14}MnSb_{11}$: new high efficiency thermoelectric material for power generation. *Chem. Mater.* **18,** 1873–1877 (2006).
16. Kurosaki, K., Kosuga, A., Muta, H., Uno, M. & Yamanaka, S. Ag_9TlTe_5: a high-performance thermoelectric bulk material with extremely low thermal conductivity. *Appl. Phys. Lett.* **87,** 061919 (2005).
17. Rhyee, J.-S. *et al.* Peierls distortion as a route to high thermoelectric performance in $In_4Se_{3-\delta}$ crystals. *Nature* **459,** 965–968 (2009).
18. Yu, J. G., Yue, A. S. & Stafsudd, O. M. Growth and electronic properties of the SnSe semiconductor. *J. Cryst. Growth* **54,** 248–252 (1981).
19. Wasscher, J. D., Albers, W. & Haas, C. Simple evaluation of the maximum thermoelectric figure of merit, with application to mixed crystals $SnS_{1-x}Se_x$. *Solid-State Electron.* **6,** 261–264 (1963).
20. Peters, M. J. & McNeil, L. E. High-pressure Mossbauer study of SnSe. *Phys. Rev. B* **41,** 5893–5897 (1990).
21. Chattopadhyay, T., Pannetier, J. & Vonschnering, H. G. Neutron-diffraction study of the structural phase-transition in SnS and SnSe. *J. Phys. Chem. Solids* **47,** 879–885 (1986).
22. Baumgardner, W. J., Choi, J. J., Lim, Y.-F. & Hanrath, T. SnSe nanocrystals: synthesis, structure, optical properties, and surface chemistry. *J. Am. Chem. Soc.* **132,** 9519–9521 (2010).
23. Morelli, D. T., Jovovic, V. & Heremans, J. P. Intrinsically minimal thermal conductivity in cubic I-V-VI_2 semiconductors. *Phys. Rev. Lett.* **101,** 035901 (2008).
24. Fultz, B. & Howe, J. M. *Transmission Electron Microscopy and Diffractometry of Materials* (Springer, 2012).
25. Nielsen, M. D., Ozolins, V. & Heremans, J. P. Lone pair electrons minimize lattice thermal conductivity. *Energ. Environ. Sci.* **6,** 570–578 (2013).
26. Zhang, Y. S. *et al.* First-principles description of anomalously low lattice thermal conductivity in thermoelectric Cu-Sb-Se ternary semiconductors. *Phys. Rev. B* **85,** 054306 (2012).
27. Slack, G. A. in *Solid State Physics* (ed. Seitz, F. *et al.*) 1–71 (Academic, 1979).
28. Clarke, D. T. Materials selection guidelines for low thermal conductivity thermal barrier coatings. *Surf. Coat. Technol.* **163–164,** 67–74 (2003).

29. Cahill, D. G., Watson, S. K. & Pohl, R. O. Lower limit to the thermal conductivity of disordered crystals. *Phys. Rev. B* **46,** 6131–6140 (1992).

Acknowledgements This work was supported in part by Revolutionary Materials for Solid State Energy Conversion, an Energy Frontier Research Center funded by the US Department of Energy, Office of Science, and Office of Basic Energy Sciences under award number DE-SC0001054 (L.-D.Z., S.-H.L., Y.Z., H.S., G.T., C.U., C.W., V.P.D. and M.G.K.). TEM work was performed in the (EPIC, NIFTI, Keck-II) facility of the NUANCE Center at Northwestern University. The NUANCE Center is supported by NSF-NSEC, NSF-MRSEC, the Keck Foundation, the State of Illinois and Northwestern University.

Author Contributions L.-D.Z. synthesized the samples, designed and carried out thermoelectric experiments, and wrote the paper. S.-H.L. and V.P.D. performed the TEM characterizations. Y.Z. carried out the calculations. H.S. and C.U. carried out the Hall measurements. G.T. helped with sample synthesis. L.-D.Z., S.-H.L., Y.Z., H.S., G.T., C.U., C.W., V.P.D. and M.G.K. conceived the experiments, analysed the results and co-edited the manuscript. S.-H.L. and Y.Z. contributed equally.

Author Information Reprints and permissions information is available at www.nature.com/reprints. The authors declare no competing financial interests. Readers are welcome to comment on the online version of the paper. Correspondence and requests for materials should be addressed to M.G.K. (m-kanatzidis@northwestern.edu).

METHODS

Starting materials. Sn chunk (99.999%, American Elements, USA) and Se shot (99.999%, 5N Plus, Canada).

Bridgman crystal growth. Ingots (~20 g) of nominal composition SnSe were synthesized by mixing appropriate ratios of high-purity starting materials (Sn and Se) in quartz tubes. The tubes were evacuated to a pressure of $\sim 10^{-4}$ torr, flame-sealed, slowly heated to 1,223 K in 10 h, soaked at this temperature for 6 h and subsequently furnace cooled to room temperature. The temperature of 1,223 K (950 °C) is determined by differential thermal analysis (DTA) of SnSe (Extended Data Fig. 9). The obtained ingots were crushed into powder and placed in a quartz tube, evacuated and flame-sealed. This charged quartz tube was placed into another, bigger, quartz tube, evacuated and flame-sealed. The outer tube is used to prevent the crystal from oxidation by air because the inner tube breaks owing to the considerable difference of thermal expansion between the crystal and quartz, near fully dense samples are achieved. SnSe crystals with dimensions of 13 mm (diameter) × 20 mm (length) were obtained. Good experimental repeatability was evidenced by seven crystals with excellent quality, in terms of showing shining flat surfaces, no cracks or obvious defects, and no porosity or other macroscopic features.

Electrical transport properties. The obtained SnSe single crystals were cut into bars along different directions with dimensions 10 mm × 2.5 mm × 2.5 mm, which were used for simultaneous measurement of the Seebeck coefficient and the electrical conductivity using an UlvacRiko ZEM-3 instrument under a helium atmosphere from room temperature to 973 K. The uncertainty of the Seebeck coefficient and electrical conductivity measurements is 5%, and is about 10% for the power factor.

Hall measurements. High-temperature Hall coefficients were measured with a custom-made high-temperature apparatus, which provides a working range from 300 to 823 K. A sample with dimensions 8 mm × 3 mm × 1 mm was mounted and protected with an argon gas atmosphere to avoid possible oxidation at high temperature. The Hall resistance was monitored with a Linear Research AC Resistance Bridge (LR-700), with constant magnetic fields of ±1 T applied by using an Oxford Superconducting Magnet.

Thermal conductivity. High-density SnSe crystals were cut and polished into coins of diameter ~8 mm (or rectangular samples with side length of 6 mm) and ~2 mm thickness for thermal diffusivity measurements along different directions. The samples were coated with a thin layer of graphite to minimize errors from the emissivity of the material. The thermal conductivity was calculated from $\kappa = DC_p\rho$, where the thermal diffusivity coefficient (D) was measured along the same direction as the electrical transport using the laser flash diffusivity method in a Netzsch LFA457, the specific heat capacity (C_p) was indirectly derived using a representative sample (Pyroceram 9606) in the range from room temperature to 973 K, and the density (ρ) was determined using the dimensions and mass of the sample and then reconfirmed using gas pycnometer (Micromeritics AccuPyc1340) measurements. The thermal diffusivity data were analysed using a Cowan model with pulse correction, and heating and cooling cycles give reproducible values for each sample. The uncertainty of the thermal conductivity is estimated to be within 5%, considering the uncertainties for D, C_p and ρ. The combined uncertainty for all measurements involved in the calculation of ZT is around 15%.

Bandgap measurements. Room-temperature optical diffuse reflectance measurements were performed on finely ground powders to probe the optical energy gap. The measurements were performed using a Shimadzu Model UV-3101PC double-beam, double-monochromator spectrophotometer (ultraviolet–visible absorption spectroscopy). $BaSO_4$ was used as a 100% reflectance standard. The generated reflectance versus wavelength data were used to estimate the bandgap by converting reflectance to absorption data according to the Kubelka-Munk equation: $\alpha/S = (1-R)^2/(2R)$, where R is the reflectance, and α and S are the absorption and scattering coefficients, respectively.

Differential thermal analysis (DTA). Differential thermal analysis was performed with a computer-controlled Shimadzu DTA-50 thermal analyser. A ground SnSe crystal (~30 mg total mass) was sealed in a fused quartz ampoule under vacuum. An ampoule containing α-Al_2O_3 of equal mass was sealed and placed on the reference side of the detector. The SnSe sample and reference were heated to 1,173 K at a rate of 3 °C min^{-1} and cooled at a rate of 3 °C min^{-1} to 50 °C. DTA measurements were run in two successive cycles of heating and cooling.

Transmission electron microscopy (TEM). Transmission electron microscope investigations were conducted with a JEOL 2100F at 200 kV. A Gatan double-tilt heating stage was used to carry out the *in situ* heating experiments. The *in situ* experiment was conducted under a fast temperature ramping rate (20 K min^{-1}) and more than 30 min sample incubation time. TEM samples were prepared by a standard conventional method with polishing, dimpling, and Ar-ion milling. Crystal Maker and Single Crystal software (CrystalMaker Software)were used to simulate the crystal structure and diffraction patterns.

Electron backscattering scatter diffraction (EBSD). The EBSD investigation was conducted using an FEI Quanta ESEM equipped with Aztec and Oxford Channel 5 software for data collection and analysis, respectively. The sample was polished until mirror-like, and data were collected from a 1 mm^2 area.

X-ray diffraction (XRD). Samples with a cleavage plane of (100) were used for XRD characterization. The XRD pattern was obtained with Cu K_α (λ = 1.5418 Å) radiation in a reflection geometry on an Inel diffractometer operating at 40 kV and 20 mA and equipped with a position-sensitive detector.

Density functional theory (DFT) calculations. We perform DFT calculations using the Vienna *Ab initio* Simulation Package (VASP)[30] with the projector augmented wave (PAW) scheme, and the generalized gradient approximation of Perdew, Burke and Ernzerhof (GGA-PBE)[31] for the electronic exchange-correlation functional. The energy cut-off for the plane wave expansion is 500 eV. The Brillouin zones of SnSe are sampled by Monkhorst-Pack[32] k-point meshes of (4 × 12 × 12). Atomic positions and unit cell vectors are relaxed until all the forces and components of the stress tensor are below 0.01 eV $Å^{-1}$ and 0.2 kbar, respectively. Vibrational properties are calculated using the supercell (112 atoms in the SnSe supercell) force constant method by the alloy theoretic automated toolkit (ATAT)[33]. In the quasiharmonic DFT phonon calculations, the system volume is isotropically expanded by +2% from the DFT relaxed volume. The Grüneisen parameter (γ) is defined as

$$\gamma_i = -\frac{V}{\omega_i}\frac{\partial \omega_i}{\partial V}$$

which characterizes the relationship between phonon frequency and volume change. The Grüneisen parameters provide an estimate of the strength of the anharmonicity in a compound. The minimum lattice thermal conductivity can be calculated using the approach developed by Cahill[34]:

$$\kappa_{\min} = \left(\frac{\pi}{6}\right)^{1/3} k_B n^{2/3} \sum_i \nu_i \left(\frac{T}{\Theta_i}\right)^2 \int_0^{\Theta_i/T} \frac{x^3 e^x}{(e^x-1)^2}\,dx$$

where ν, Θ and n are the phonon velocity, Debye temperature and the number density of atoms, respectively.

The crystal structure of SnSe at low temperature has a *Pnma* space group, with a = 11.58 Å, b = 4.22 Å and c = 4.40 Å. Increasing the temperature to 800 K, SnSe undergoes a phase transition from the low-temperature *Pnma* phase to the high-temperature *Cmcm* phase. In the *Cmcm* phase, the experimentally measured lattice constants are a = 4.31 Å, b = 11.71 Å and c = 4.31 Å (refs 35, 36). Our theoretically relaxed low-temperature and high-temperature SnSe lattice constants are respectively a = 11.794 Å, b = 4.215 Å and c = 4.550 Å, and a = 4.30 Å, b = 12.08 Å and c = 4.30 Å, which are in good agreement with the experimental measurements. The theoretically calculated electronic band structures of low-temperature and high-temperature SnSe phases are shown in Extended Data Fig. 4a, b. The theoretically calculated bandgap of the low-temperature SnSe phase is 0.61 eV, which is smaller than the experimentally measured 0.86 eV (Extended Data Fig. 5). Underestimation of bandgaps in the DFT framework is a well-known problem in the community. Even though DFT does not give quantitatively accurate predictions of bandgaps, the trends of bandgap between different phases are more reliable. The band structures show some features that suggest potential for thermoelectric materials: such as flattened valence bands and degenerate band extrema at off-Γ points. For the high-temperature SnSe phase (Extended Data Fig. 4b), the theoretically calculated bandgap is 0.39 eV (it is experimentally difficult to measure), which is much lower than that of the low-temperature phase. The smaller bandgap at high-temperature is in good agreement with the experimentally observed reduction of the Seebeck coefficient and the rise in electrical conductivity at high temperatures.

30. Kresse, G. & Joubert, D. From ultrasoft pseudopotentials to the projector augmented-wave method. *Phys. Rev. B* **59,** 1758–1775 (1999).
31. Perdew, J. P., Burke, K. & Ernzerhof, M. Generalized gradient approximation made simple. *Phys. Rev. Lett.* **77,** 3865–3868 (1996).
32. Monkhorst, H. J. & Pack, J. D. Special points for Brillouin-Zone integrations. *Phys. Rev. B* **13,** 5188–5192 (1976).
33. van de Walle, A., Asta, M. & Ceder, G. The alloy theoretical automated toolkit: a user guide. *Calphad* **26,** 539–553 (2002).
34. Cahill, D. G., Watson, S. K. & Pohl, R. O. Lower limit to the thermal conductivity of disordered crystals. *Phys. Rev. B* **46,** 6131–6140 (1992).
35. Chattopadhyay, T., Pannetier, J. & Vonschnering, H. G. Neutron-diffraction study of the structural phase-transition in SnS and SnSe. *J. Phys. Chem. Solids* **47,** 879–885 (1986).
36. Baumgardner, W. J., Choi, J. J., Lim, Y.-F. & Hanrath, T. SnSe nanocrystals: synthesis, structure, optical properties, and surface chemistry. *J. Am. Chem. Soc.* **132,** 9519–9521 (2010).

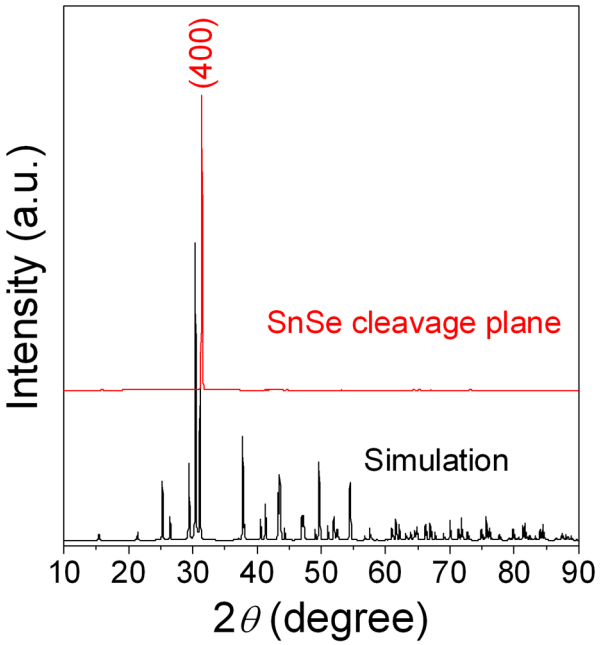

Extended Data Figure 1 | XRD measurement of SnSe on the cleavage plane, and the simulated diffraction pattern. The (400) reflection plane indicates that the SnSe crystal is cleaved at the plane that is perpendicular to the *a* axis.

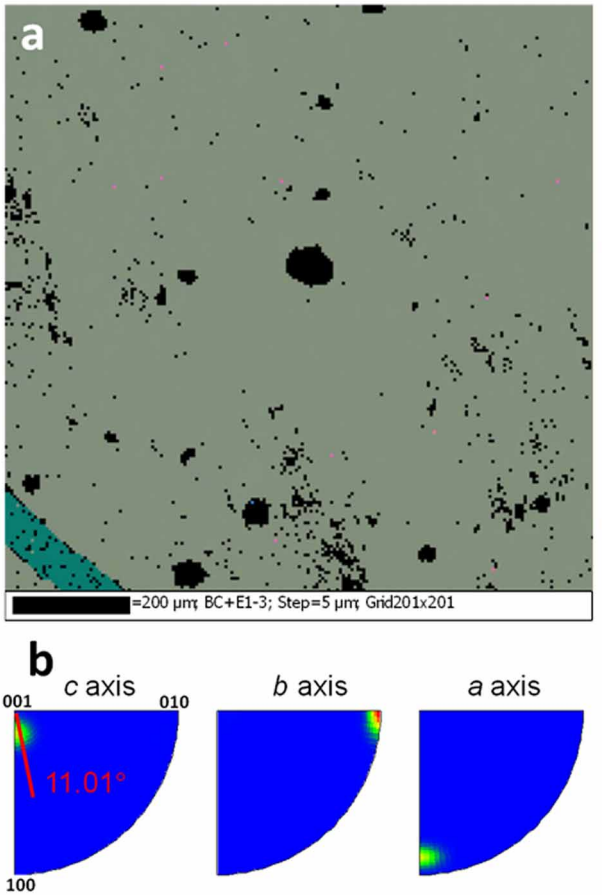

Extended Data Figure 2 | EBSD analysis on a 1 mm^2 surface. **a**, The all-Euler map showing a large area of sample surface with homogeneous orientation. **b**, The inverse pole figures of samples cut along the *a*–*b*, *c*–*a* and *b*–*c* planes, respectively. The view down the *c*-axis (left figure) indicates a slight deviation (~11°) from it. Scale bar, 200 µm.

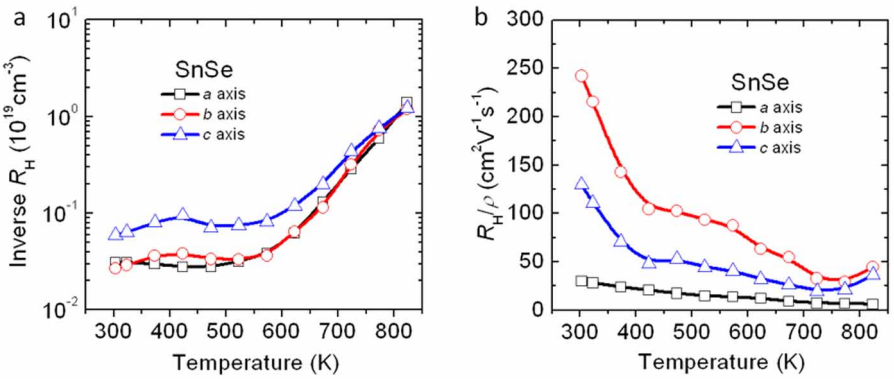

Extended Data Figure 3 | Hall transport properties of crystalline SnSe. **a**, Inverse R_H (R_H, Hall coefficient), and **b**, R_H/ρ (ρ, electrical resistivity) of SnSe crystals along different axial directions. Inverse R_H gives an indication of the carrier concentration; R_H/ρ is related to the carrier mobility.

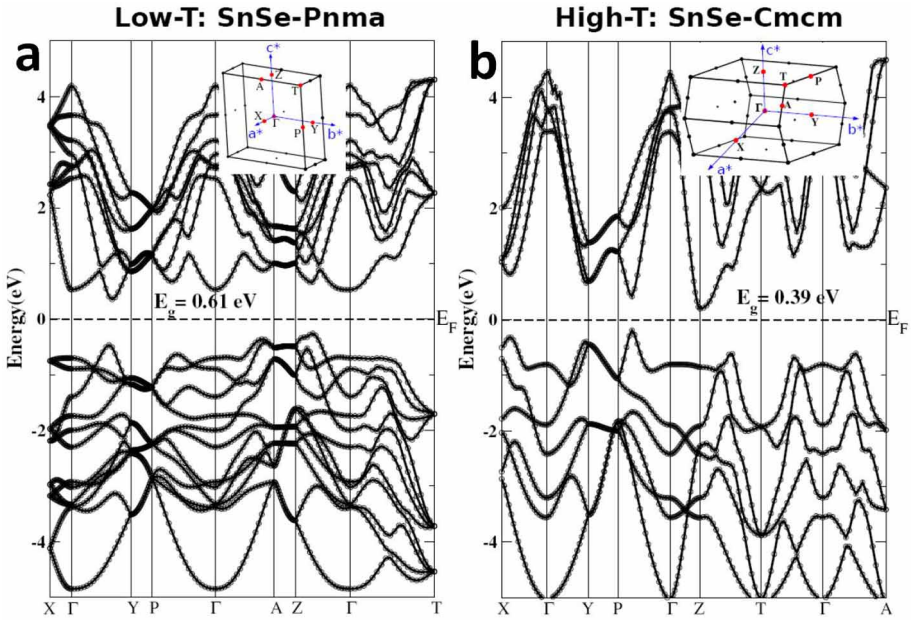

Extended Data Figure 4 | Electronic band structures of low-temperature (*Pnma*) and high-temperature (*Cmcm*) phases of SnSe. **a**, SnSe at low temperature (Low-T) with the *Pnma* space group. **b**, SnSe at high temperature (High-T) with the *Cmcm* space group. The dashed lines indicate the position of the Fermi level (E_F). Inset figures are the first Brillouin zones (BZ) of SnSe with high-symmetry points (red points) that we considered in our band structure calculations. Both phases are indirect-bandgap (E_g) compounds. For the low-temperature phase, the indirect bandgap is along ΓY in its BZ; for the high-temperature phase, the indirect bandgap is from a point within the ΓP direction to the Z point in its BZ.

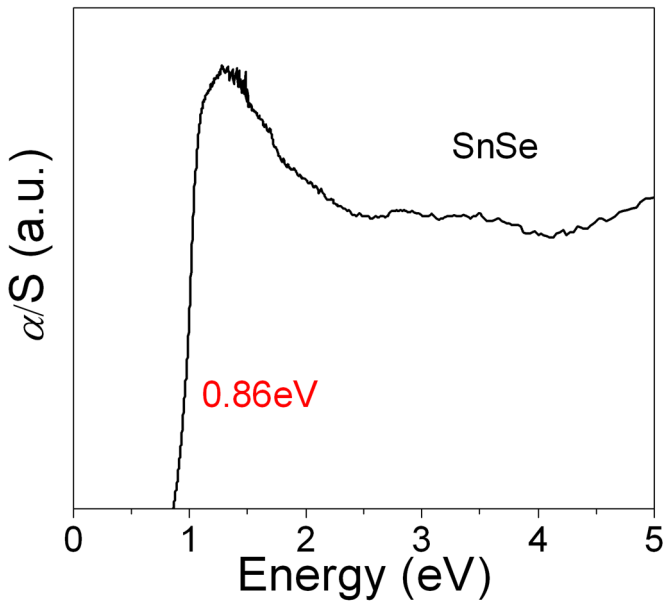

Extended Data Figure 5 | Bandgap of SnSe at room temperature. Optical absorption spectrum (black trace) and energy bandgap (*x*-axis intercept) indicate a bandgap of 0.86 eV (red) of SnSe at room temperature. See Methods for details of α and *S*.

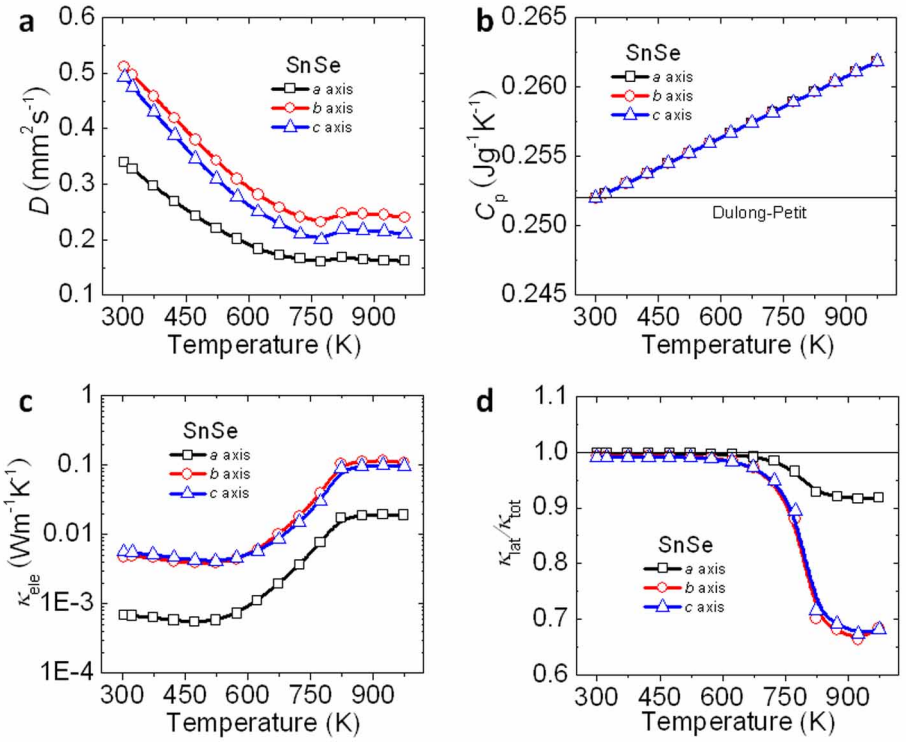

Extended Data Figure 6 | Thermoelectric properties as a function of temperature for crystalline SnSe along different directions. **a**, Thermal diffusivity. **b**, Heat capacity. **c**, Electronic thermal conductivity. **d**, The ratio of lattice thermal conductivity (κ_{lat}) to total thermal conductivity (κ_{tot}). The Lorenz number (L) used for obtaining κ_{lat} ($\kappa_{lat} = \kappa_{tot} - \sigma LT$, where σ is the electrical conductivity and T is absolute temperature) was approximately equal to $1.5 \times 10^{-8}\,V^2\,K^{-2}$ since the undoped SnSe is a non-degenerate semiconductor; the ratio of κ_{lat} to κ_{tot} indicates that κ_{tot} is dominated by phonon transport.

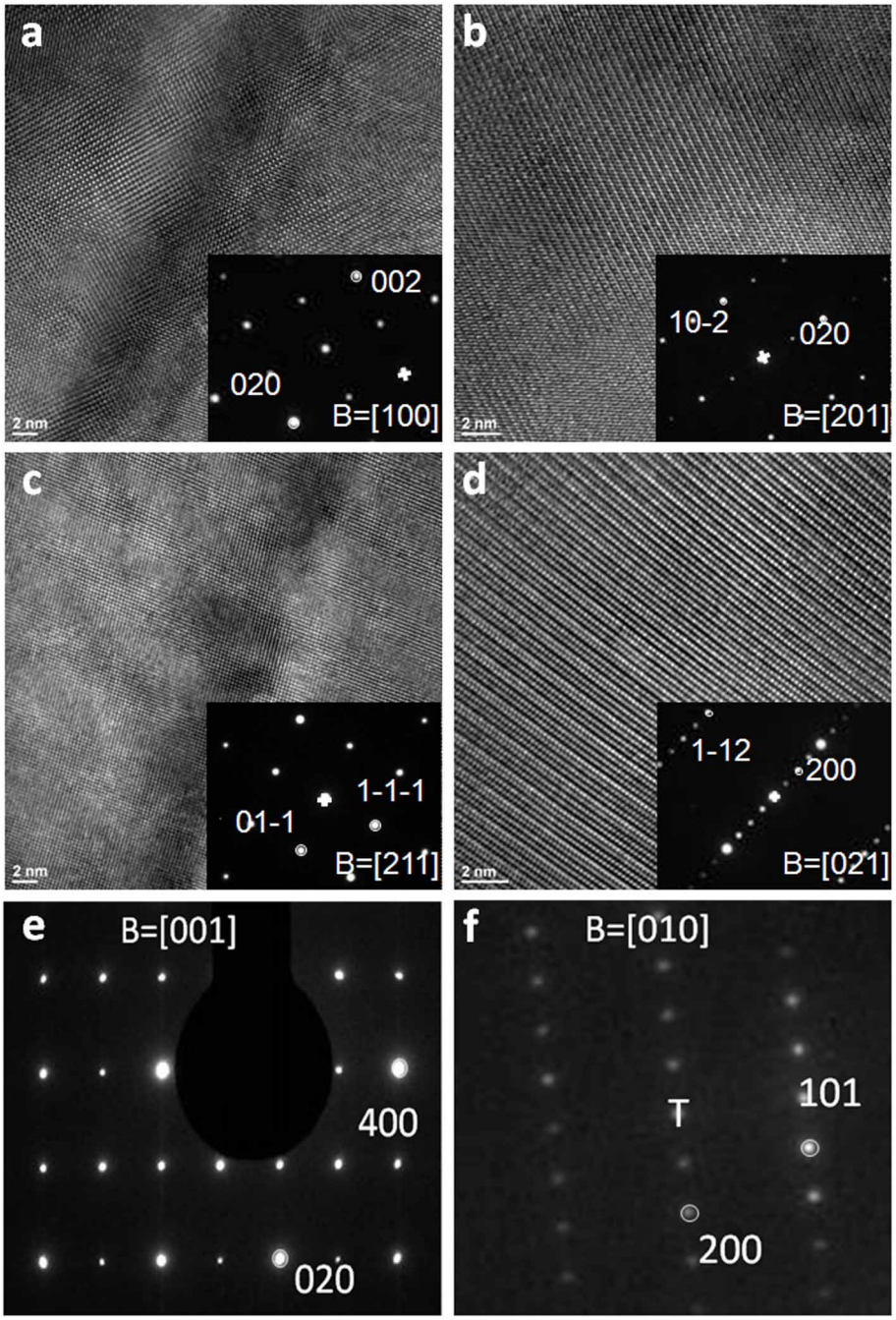

Extended Data Figure 7 | High-resolution TEM images of single-crystal SnSe along four zone axes, and SAD along a low-order zone axis (in insets). **a**, Along the [100] direction. **b**, Along the [201] direction. **c**, Along the [211] direction. **d**, Along the [021] direction. **e**, Electron diffraction pattern along the [001] direction. **f**, Electron diffraction pattern along the [010] direction. The combination of all six figures provides strong evidence of the single-crystal orthorhombic layered structure of SnSe.

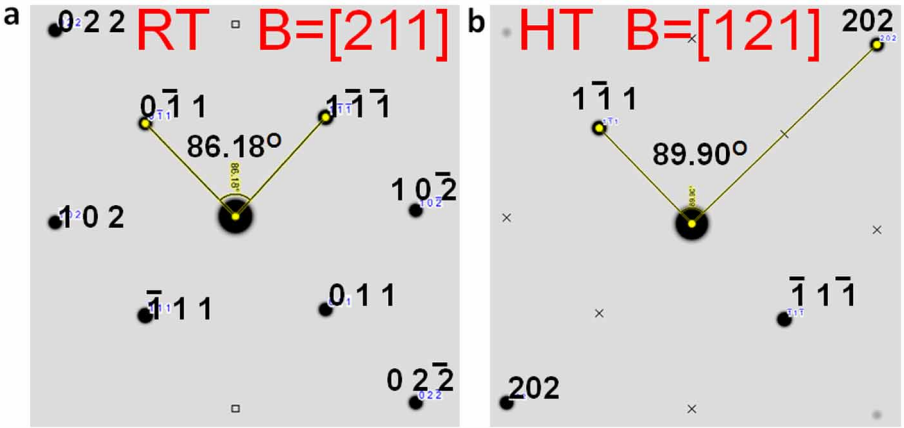

Extended Data Figure 8 | Simulated SADs for SnSe. **a**, Room-temperature (RT; *Pnma*) phase; **b**, high-temperature (HT; *Cmcm*) phase. B, zone axis. Note $\bar{1}$ is used here to indicate -1.

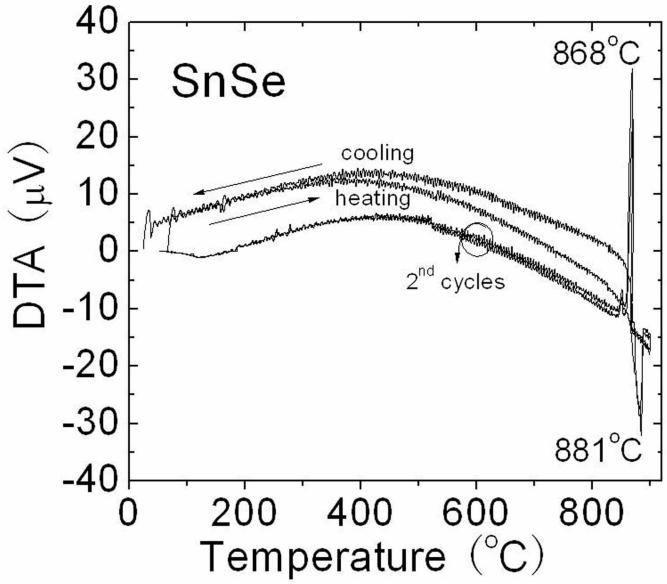

Extended Data Figure 9 | Differential thermal analysis of SnSe. DTA measurements showing two heating and cooling cycles. DTA results indicate that SnSe appears to melt congruently; one endothermic peak is observed at 881 °C on the heating curve and one exothermic peak is observed at 868 °C on the cooling curve. Two heating–cooling cycles indicate the same melting and crystallization point for a given sample, consistent with high purity. Heat flow is represented as a μV signal, plotted on the *y* axis.

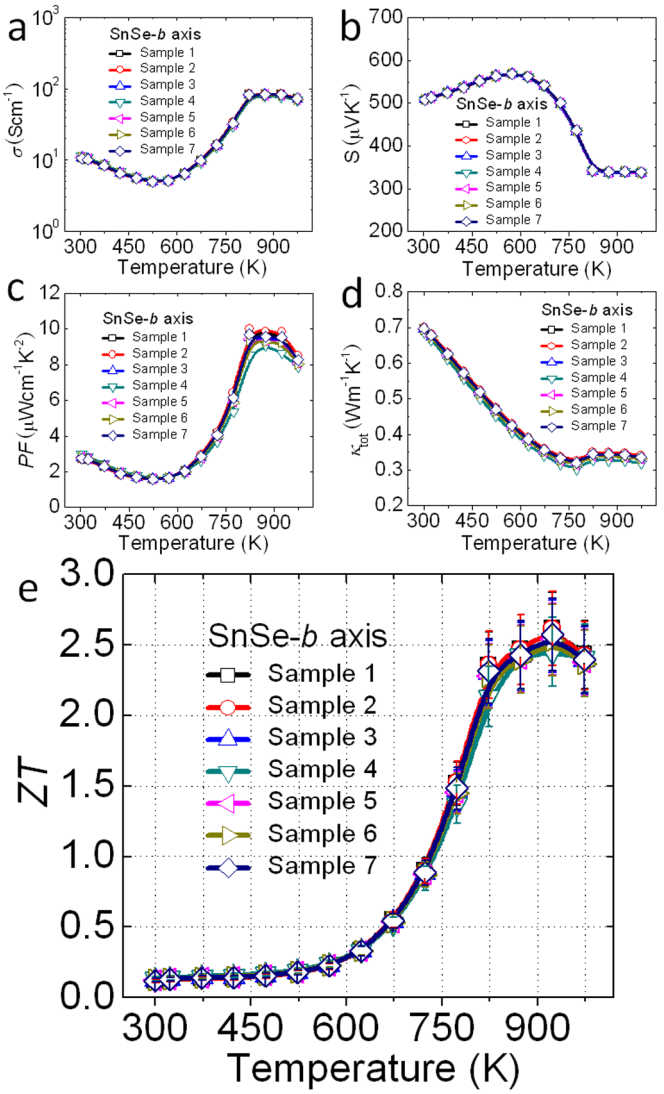

Extended Data Figure 10 | Reproducibility, and thermoelectric properties as a function of temperature, for seven samples of SnSe crystals along the *b* axis. **a**, Electrical conductivity. **b**, Seebeck coefficient. **c**, Power factor. **d**, Total thermal conductivity. **e**, *ZT*; error bars are ±15%.

Extended Data Table 1 | Transverse (TA/TA') and longitudinal (LA) Debye temperatures (Θ), phonon velocities (v) and Grüneisen parameters (γ) along *a*, *b* and *c* axes in the low-temperature SnSe phase.

Γ*X*/*a*	Θ(K)	*v* (m/s)	γ
TA	19	955	5.1
TA'	24	1194	1.1
LA	29	2117	5.9
Average	24	1422	4.1
Γ*Y*/*b*			
TA	62	1279	2.7
TA'	72	1850	2.4
LA	62	2878	1.3
Average	65	2002	2.1
Γ*Z*/*c*			
TA	53	1467	1.0
TA'	68	1903	2.7
LA	53	2072	3.3
Average	58	1814	2.3

Values are calculated from the phonon and Grüneisen dispersions (Fig. 4a, b). The Debye temperature is calculated using $\Theta = \omega_D/k_B$ (ω_D is the largest acoustic frequency in each direction); the phonon velocity is the slope of the acoustic phonon dispersion around the Γ point; the Grüneisen parameter of each acoustic dispersion is evaluated from the root-mean-square value of γ_i along each direction: $\gamma = \sqrt{<\gamma_i^2>}$. Additionally, average acoustic values of Debye temperatures, phonon velocities and Grüneisen parameters are given, which are the above quantities, averaged over the three acoustic branches.